JOURNAL OF GEOPHYSICAL RESEARCH: SOLID EARTH, VOL. 118, 5030–5039, doi:10.1002/jgrb.50347, 2013

Geodetic investigation into the deformation of the Salton Trough

Brendan W. Crowell,[1,2] Yehuda Bock,[1] David T. Sandwell,[1] and Yuri Fialko[1]

Received 14 February 2013; revised 16 August 2013; accepted 20 August 2013; published 11 September 2013.

[1] The Salton Trough represents a complex transition between the spreading center in Baja California and the strike-slip San Andreas fault system and is one of the most active zones of deformation and seismicity in California. We present a high-resolution interseismic velocity field for the Salton Trough derived from 74 continuous GPS sites and 109 benchmarks surveyed in three GPS campaigns during 2008–2009 and previous surveys between 2000 and 2005. We also investigate small-scale deformation by removing the regional velocity field predicted by an elastic block model for Southern California from the observed velocities. We find a total extension rate of 11 mm/yr from the Mesquite Basin to the southern edge of the San Andreas Fault, coupled with 15 mm/yr of left-lateral shear, the majority of which is concentrated in the southern Salton Sea and Obsidian Buttes and is equivalent to 17 mm/yr oriented in the direction of the San Andreas Fault. Differential shear strain is exclusively localized in the Brawley Seismic Zone, and dilatation rate indicates widespread extension throughout the zone. In addition, we infer clockwise rotation of 10°/Ma, consistent with northwestward propagation of the Brawley Seismic Zone over geologic time.

Citation: Crowell, B. W., Y. Bock, D. T. Sandwell, and Y. Fialko (2013), Geodetic investigation into the deformation of the Salton Trough, *J. Geophys. Res. Solid Earth*, *118*, 5030–5039, doi:10.1002/jgrb.50347.

1. Introduction

[2] The Salton Trough lies at the transition from the spreading centers of the Gulf of California and East Pacific Rise to the south into the predominately strike-slip San Andreas fault system to the north and is a classic example of a transtensional basin. The historical and paleoseismic records show that the San Andreas Fault in California experiences great earthquakes every 150 years on average; however, the southernmost segment of the San Andreas is the only seismogenic part of the fault that has not ruptured in historic times and is approaching or exceeding the maximum slip deficit known from paleoseismic studies along this part of the fault [*Fialko*, 2006]. The threat of a large earthquake on the southern terminus of the San Andreas Fault has generated increased interest in the seismotectonics of the Salton Trough. *Brothers et al*. [2011] showed that slip along conjugate faults in the Salton Sea causes an appreciable change in Coulomb stress along the southern San Andreas Fault, making full characterization of deformation in the Brawley Seismic Zone necessary for hazard assessment. The Imperial Fault, at the southern end of the Imperial Valley, is a fast-moving and partially creeping fault that accommodates most of the relative motion between the North American and Pacific plates at that latitude, roughly 40 mm/yr [*Genrich et al*., 1997; *Lyons et al*., 2002], and also has been the location for many large earthquakes (e.g., 1940 M_w 7.1 and 1979 M_w 6.4 [*Archuleta*, 1982]). From the terminus of the Imperial Fault and other auxiliary faults such as the Brawley and Superstition Hills Faults, there exists a large step over to the San Andreas Fault. Many parallel oblique normal N15°E striking faults help bridge the gap between the faults [*Brothers et al*., 2009]. Large-scale subsidence and anomalous heat flow exist in the Imperial Valley near Obsidian Buttes and Mexico's Cerro Prieto volcanic zone caused by both tectonic extension and water extraction for irrigation and geothermal plants [*Lachenbruch et al*., 1985; *Lynch and Hudnut*, 2008].

[3] Seismically, the region is one of the most active in California, with many small swarms of earthquakes such as the 1982 West Moreland, the 2005 Obsidian Buttes, the 2009 Bombay Beach, and the 2012 Brawley seismic swarms [*Shearer*, 2002; *Lohman and McGuire*, 2007; *Chen and Shearer*, 2011]. Recent moderate-to-large earthquakes include the 1987 M_w 6.6 Superstition Hills and M_w 6.2 Elmore Ranch earthquakes that occurred 1 day apart [*Hanks and Allen*, 1989], the 1954 M_w 6.4 San Jacinto earthquake [*Sharp*, 1967], the 1968 M_w 6.5 Borrego Mountain earthquake [*Burford*, 1972], and the 2010 M_w 7.2 El Mayor-Cucapah earthquake [*Hauksson et al*., 2011].

[4] A detailed picture of crustal motion and strain accumulation in this complex tectonic region requires geodetic measurements with high spatial density. The Imperial and Coachella Valleys are both locations of intense agricultural activity resulting in temporal decorrelation in Interferometric Synthetic Aperture Radar (InSAR) [*Lohman and McGuire*, 2007]. Persistent scattering methods have been partially successful in the areas north of the Salton Sea but less effective

Additional supporting information may be found in the online version of this article.

[1]Cecil H. and Ida M. Green Institute of Geophysics and Planetary Physics, Scripps Institution of Oceanography, University of California San Diego, La Jolla, California, USA.

[2]Now at Department of Earth and Space Sciences, University of Washington, Seattle, Washington, USA.

Corresponding author: B. W. Crowell, Department of Earth and Space Sciences, University of Washington, Johnson Hall Rm-070, Box 351310, 4000 15th Ave. NE, Seattle, WA 98195-1310, USA. (crowellb@uw.edu)

2169-9313/13/10.1002/jgrb.50347

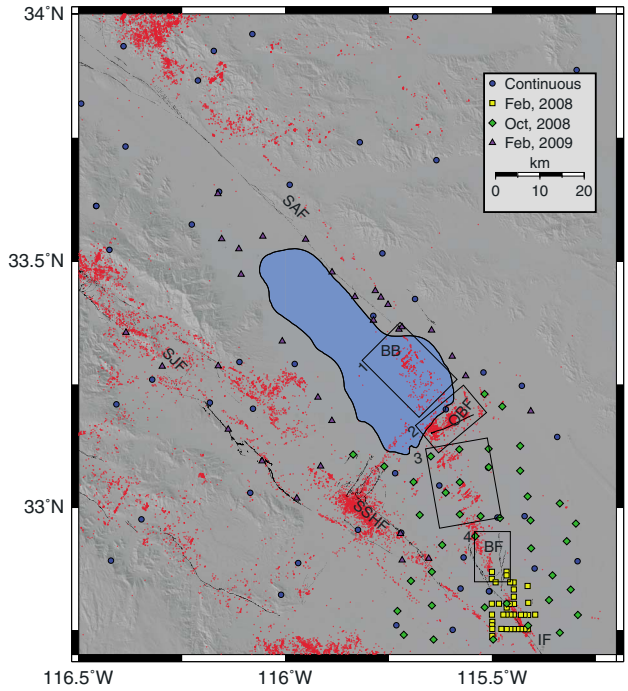

Figure 1. Locations of continuous and campaign GPS monuments in the Salton Trough. The boxes represent the four main study areas: the southern Salton Sea (1), Obsidian Buttes (2), the Central Brawley Seismic Zone (3), and the Mesquite Basin (4). SAF, San Andreas Fault; SJF, San Jacinto Fault; SSHF, Superstition Hills Fault; OBF, Obsidian Buttes Fault; BF, Brawley Fault; IF, Imperial Fault; BB, Bombay Beach. The red dots are all earthquakes greater than *M*2 from the *Lin et al*. [2007] catalog.

to the south [*Lyons and Sandwell*, 2003]. A significant number of continuous Global Positioning System (GPS) stations have been installed in this region, but the average spacing between the continuous GPS monuments is ~20 km, so local GPS surveying is the only feasible option for resolving small-scale deformation in this area. To increase the spatial density of measurements, we conducted three surveys in the Salton Trough, from the United States-Mexico border into the Coachella Valley to the north. We also used data from previous surveys performed in the early summers of 2000, 2003, 2004, and 2005 to compute station velocities. After creating a velocity field, we computed baseline length changes across regions of high deformation in the Salton Trough and determined the amount of motion through four provinces: the southern Salton Sea, Obsidian Buttes, the Central Brawley Seismic Zone, and the Mesquite Basin. We also removed a component of regional tectonics using a block model [*Smith-Konter and Sandwell*, 2009] to look at local deformation caused just by auxiliary faulting. To look in more detail at internal deformation, we computed strain rates from the velocity fields throughout the Salton Trough, which helps us characterize the amount of shear, dilatation, and rotation throughout. We also present an analysis of vertical deformation from continuous GPS to complement the extension measurements in the Salton Trough, and argue that the available data indicate the northwestward propagation of the Brawley Seismic Zone.

2. Data

2.1. Campaign GPS Surveys and Processing

[5] We performed three campaign GPS surveys in February 2008, October 2008, and February 2009 (Figure 1). During each survey, teams autonomously surveyed a subset of sites at least twice during each campaign. Each occupation was between 12 and 20 min at a 1 s sampling rate. Occupations of the same monument were performed at different times during the day, approximately 6 and 18 h away from the first occupation, to obtain a different satellite set to reduce multipath errors. Using the method of instantaneous relative positioning [*Bock et al*., 2000], we were able to carry out the surveys in a rapid and efficient manner so that many monuments could be surveyed with modest manpower and processed on-the-fly with respect to continuous GPS stations in the California Real Time Network (CRTN) (http://sopac.ucsd.edu/projects/realtime/CRTN/). Raw receiver data, either from Leica GMX902 or Ashtech Z-X113 GPS receivers, were streamed via Bluetooth protocol to Verizon XV6700 smartphones running Geodetics, Inc. RTD Rover software. The raw data were streamed to a server at the Scripps Orbit and Permanent Array Center (SOPAC), where positions were computed using the International Terrestrial Reference Frame (ITRF) 2005 [*Altamimi et al*., 2007] coordinates of the CRTN stations valid for that day, ultrarapid SOPAC orbital parameters (http://garner.ucsd.edu/pub/products), and the NOAA Tropospheric Signal Delay Model (NOAATrop) [*Gutman et al*., 2004]. Positions and statistics were then streamed back to the user where they were stored on the memory card of the smartphone. Raw receiver data were stored on the server as well as the memory card for postprocessing. For this study, postprocessing was done after IGS final orbits became available.

[6] The February 2008 survey consisted of 34 geodetic monuments established by Imperial College, London [*Mason*, 1987] and four National Geodetic Survey (NGS) sites centered on the Imperial Fault. Previous GPS surveys of this dense array of monuments occurred in 1991, 1993, 1999, and 2000 [*Genrich et al*., 1997; *Lyons et al*., 2002]. The surveys in 1999 and 2000 [*Lyons et al*., 2002] were processed through the method of instantaneous positioning with respect to the ITRF 1996 reference frame [*Sillard et al*., 1998], and the earlier surveys were processed with the GAMIT software [*Herring et al*., 2010]. For the purposes of this study, we only use data collected after 1999 [*Lyons et al*., 2002] since the earlier studies are affected by coseismic motions from the 1999 Hector Mine earthquake; other monuments surveyed only have data after 1999. We transformed these positions into the ITRF 2005 reference frame [*Altamimi et al*., 2007] prior to computing velocities.

[7] In October 2008, a survey of stations throughout the Imperial Valley was performed, encompassing the Imperial Fault and the Brawley Seismic Zone. Of the 43 monuments surveyed, 23 were National Geodetic Survey (NGS) and 20 were monuments installed in 2004 by the California Department of Transportation (Caltrans) and only surveyed once before. The Caltrans stations greatly increased the density throughout the Brawley Seismic Zone. The survey in February 2009 extended the October 2008 survey from the Brawley Seismic Zone into the Coachella Valley along both sides of the Salton Sea and consisted of 28 stations, 18 from the NGS and 10 from the U.S. Geological Survey (USGS). The survey in October 2008 consisted of stations surveyed previously in

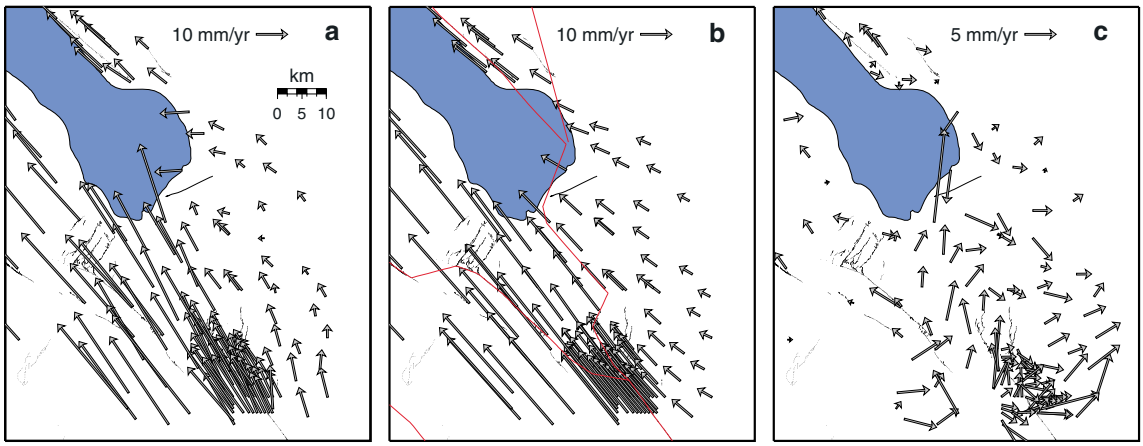

Figure 2. Interseismic velocity fields from (a) campaign and continuous GPS measurements, (b) the block model of *Smith-Konter and Sandwell* [2009], and (c) the difference between the two. The outlines of the blocks used in the block model of *Smith-Konter and Sandwell* [2009] are shown in Figure 2b.

2004. The 2004 occupations were done at a 15 s sampling rate, and generally, occupations were between 10 and 15 min. The survey in February 2009 occupied sites that were previously surveyed in 2000, 2003, 2004, or 2005. There were five NGS monuments surveyed in 2000 in the Coachella Valley and three NGS monuments surveyed in 2003 near the southern terminus of the San Andreas Fault that we resurveyed in 2009. The 2000 and 2003 data were at a 15 s sampling rate and consisted of longer occupations (15–30 min) than the 2004 data. There were 10 NGS stations that we surveyed in February 2009 that were previously surveyed in 2004. These stations were missed during the October 2008 survey. We resurveyed 10 monuments installed in 2005 by the USGS that are within a few kilometers of the San Andreas, San Jacinto, and Superstition Hills Faults. Data from these monuments were at a sampling rate of once per second and, in many cases, consisted of occupations many hours long. We postprocessed the 2003, 2004, and 2005 data through instantaneous positioning and combined the occupations using DeLorme's GeoSpider network adjustment program using the true-of-date positions of nearby continuous GPS stations as reference stations.

[8] Velocities were computed with respect to the ITRF 2005 reference frame [*Altamimi et al.*, 2007] and then corrected for North American plate motion through an Euler pole calculation. The one-sigma uncertainties on the velocity measurements are simply defined as

$$\sigma_{N,E} = \frac{\sqrt{\sigma_{N1,E1}^2 + \sigma_{N2,E2}^2}}{t} \quad (1)$$

where $\sigma_{N,E}$ are the velocity uncertainties, $\sigma_{N1,E1}$ and $\sigma_{N2,E2}$ are the individual positional uncertainties, and t is the time between observations in years [*Lyons et al.*, 2002]. Although the cross covariances between north and east components have been neglected, the positional variances have been adjusted to account for the temporal correlations in the GPS observations [*Genrich and Bock*, 2006]. The velocities and uncertainties are shown in the supporting information.

2.2. Continuous GPS Processing

[9] Over 1800 stations in western North America were, at the time of this study, processed daily at SOPAC using the GAMIT/GLOBK package [*Herring et al.*, 2010] with respect to the ITRF 2005 reference frame. For this study, we utilize 74 continuous GPS stations around the Imperial Valley and estimate velocities between 2000 and 2010 through least squares. We exclude postseismic terms and fit only a linear trend and annual and semiannual terms since we are interested in the actual velocities during the time period, rather than the estimated interseismic velocities that are computed through a superposition of many model terms. Nonlinear transient effects in this area from the 1999 Hector Mine earthquake are negligible after ~2001, so it is reasonable to ignore them. The model fit produces velocities that are similar to the campaign velocities since only a simple linear trend is fit to those data. After velocities are computed, we perform the same Euler pole correction used for the campaign measurements to put the velocities in the local reference frame. The velocities and uncertainties are shown in the supporting information.

3. Methods

3.1. Extensional Baseline Measurements

[10] The observed velocity field can be represented as the superposition of a regional velocity field and a local velocity field. The regional field is due to large-scale tectonics and is dominated by the relative motion between the Pacific and North American plates. The local field is the result of conjugate faulting, fault edge effects, hydrological signals, and diffuse (i.e., not related to any major faults) deformation. Since the velocity field is dominated by the regional field, in order to isolate the local component, we remove the regional field from the total velocity field. We take the block model solution of *Smith-Konter and Sandwell* [2009] for Southern California as a proxy for the regional velocity field. The block model is a good approximation for the regional velocity field because it incorporates only the large-scale features, leaving features associated with conjugate faulting, extension, and crustal thinning in the Salton Trough. The surface velocities computed in the block model are caused by steady slip along deep dislocations, with different locking depths assigned for each segment (block boundaries shown on Figure 2b) and described in detail in *Smith-Konter and Sandwell* [2009]. Elastic deformation in

the upper crust is also considered in the block model. Figure 2 shows the total, regional, and local velocity fields. Of note is that velocities in the far field go to zero in the local velocity field, indicating that the block model is able to remove large-scale tectonic features while leaving the more complicated local effects.

[11] Horizontal baselines are computed between pairs of stations that traverse lines of seismicity and known faulting using the local velocity field. The four major regions we are concerned about are the southern Salton Sea, Obsidian Buttes, the Central Brawley Seismic Zone, and the Mesquite Basin (Figure 1, regions 1–4, respectively). These four regions make up the Brawley Seismic Zone. We rotate the baselines into fault-parallel and fault-perpendicular directions to obtain the strike-slip and extensional motions throughout the region. In the southern Salton Sea, the Bombay Beach seismic swarms of 2001 and 2009 were along planes striking N43°E to N57°E, respectively [*Chen and Shearer*, 2011]. Seismic reflection data obtained along the floor of the Salton Sea show the existence of N15°E striking faults; however, events on these structures are thought to be infrequent [*Brothers et al.*, 2009]. *Lohman and McGuire* [2007] show from seismic relocations during the 2005 Obsidian Buttes seismic swarm that the predominant strike on the Obsidian Buttes Fault is N35°E with a dip of 72°, which is similar to the migration pattern from *Chen and Shearer* [2011] (N20°E–N66°E). However, field observations of surface offsets indicate a strike of N65°E (fault trace on Figure 1 near Obsidian Buttes Fault), while the strike of geothermal plants is between N50°E and N55°E. For computing baseline length changes, we choose N65°E to correspond with our field observations. Predominant fault planes in the Central Brawley Seismic Zone (swarms in 1983, 1986, 1999, 2008, and 2012) and Mesquite Basin (swarms in 1983, 2000, and 2003) are highly variable, although the most common orientation is about N40°E for the Central Brawley Seismic Zone and N50°E for the Mesquite Basin [*Chen and Shearer*, 2011].

[12] After the baselines are computed and rotated into their fault-parallel and fault-perpendicular directions, we compute a weighted mean of the baselines to determine the deformation of the area. The weighted mean is defined as

$$\overline{b} = \frac{\sum_{i=1}^{n} \sigma_i^{-1} b_i}{\sum_{i=1}^{n} \sigma_i^{-1}} \tag{2}$$

where b are the baseline measurements and σ are the baseline velocity standard deviations (the sum of the individual station standard deviations in the baseline). This in essence gives greater weight to baselines with two continuous GPS stations which are more reliable than baselines between campaign GPS sites. Uncertainties in subsidence and dip-slip rates are computed using an assumed 2° uncertainty on the dip angle.

3.2. Strain Rate Computation

[13] In addition to baseline velocity changes, we also compute the velocity gradient tensor over a 0.1° grid following a least squares solution using both the block model velocity field (interpolated onto observation points) and our velocity field from campaign and continuous GPS measurements. These two strain rate fields are then differenced which allows us to appropriately locate where differential strain is being accumulated throughout the Salton Trough. GPS velocity at a given point can be written as

$$u_i = t_i + \frac{\partial u_i}{\partial x_j}\Delta x_j = t_i + L_{ij}\Delta x_j \tag{3}$$

where indexes i and j correspond to spatial coordinates, t_i is translation with respect to the reference frame, L_{ij} is the velocity gradient tensor, u_i are the individual GPS velocities, and Δx_j is the baseline between each station and the grid point [*Shen et al.*, 1996; *Allmendinger et al.*, 2007]. The velocity gradient tensor in two dimensions can be decomposed into a symmetric and antisymmetric component such that

$$L = \begin{bmatrix} \frac{\partial u_x}{\partial x} & \frac{1}{2}\left(\frac{\partial u_x}{\partial y} + \frac{\partial u_y}{\partial x}\right) \\ \frac{1}{2}\left(\frac{\partial u_y}{\partial x} + \frac{\partial u_x}{\partial y}\right) & \frac{\partial u_y}{\partial y} \end{bmatrix} + \begin{bmatrix} 0 & \frac{1}{2}\left(\frac{\partial u_x}{\partial y} - \frac{\partial u_y}{\partial x}\right) \\ \frac{1}{2}\left(\frac{\partial u_y}{\partial x} - \frac{\partial u_x}{\partial y}\right) & 0 \end{bmatrix} \tag{4}$$

$$L = E + \Omega = \begin{bmatrix} e_{xx} & e_{xy} \\ e_{yx} & e_{yy} \end{bmatrix}. \tag{5}$$

[14] In equation (5), E is the strain rate tensor, Ω is the rotation rate tensor, and e_{ij} are components of the velocity gradient tensor, $e_{ij} = \frac{\partial u_i}{\partial x_j}$. To solve for the velocity gradient tensor, we set up the following inverse problem

$$u = \begin{bmatrix} u_x^1 \\ u_y^1 \\ \vdots \\ u_x^n \\ u_y^n \end{bmatrix} = Gl = \begin{bmatrix} 1 & 0 & \Delta x_1 & \Delta y_1 & 0 & 0 \\ 0 & 1 & 0 & 0 & \Delta x_1 & \Delta y_1 \\ & & & \vdots & & \\ 1 & 0 & \Delta x_n & \Delta y_n & 0 & 0 \\ 0 & 1 & 0 & 0 & \Delta x_n & \Delta y_n \end{bmatrix} \begin{bmatrix} t_x \\ t_y \\ e_{xx} \\ e_{xy} \\ e_{yy} \\ e_{yx} \end{bmatrix} \tag{6}$$

where G is the design matrix, l is a vector containing the velocity gradient and translation terms from equation (3), and n is the number of GPS stations. We follow the example of *Allmendinger et al.* [2007] in Gaussian distance weighting each station-grid pair by

$$W = \exp\left(\frac{-d^2}{2\alpha^2}\right) \tag{7}$$

where α is a constant that controls the decay and d is the distance between the grid point and the station. Grid distance weighting gives a higher weight to stations that are close to the grid point and effectively ignores stations far away. For this study, we use $\alpha = 7$ km, which is the average distance of the closest station to each grid point. Additionally, we also weigh continuous stations by a factor of 2 over campaign stations since we are more confident in the continuous velocities. We then solve for the vector l (equation (6)) through linear least squares

$$l = \left[G^T W G\right]^{-1} G^T W u. \tag{8}$$

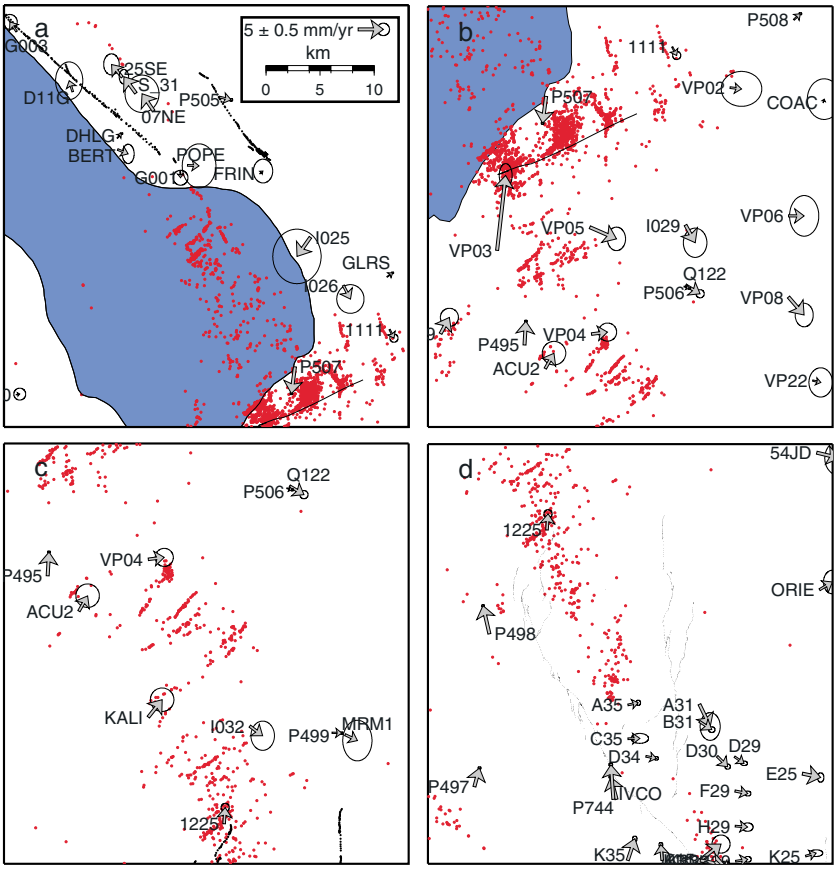

Figure 3. The local velocity field (total field minus block model) used for computing baseline length changes for the four regions of interest: (a) The southern Salton Sea, (b) Obsidian Buttes, (c) the Central Brawley Seismic Zone, and (d) the Mesquite Basin. The red dots are all earthquakes greater than *M*2 from the *Lin et al.* [2007] catalog. Error ellipses are plotted at the 95% confidence level.

[15] The shear strain rate is defined as the off-diagonal term of the strain rate tensor (equation (4))

$$E_{xy} = \frac{1}{2}\left(e_{xy} + e_{yx}\right), \tag{9}$$

and the principal components of strain rate are

$$E_{1,2} = \frac{\left(e_{xx} + e_{yy}\right)}{2} \pm \sqrt{\frac{\left(e_{xx} - e_{yy}\right)^2}{4} + \left(E_{xy}\right)^2}. \tag{10}$$

[16] The maximum shear strain rate is given by the difference between the principal strain rates,

$$E_{xy}^{\mathrm{MAX}} = \frac{E_1 - E_2}{2}. \tag{11}$$

[17] The dilatation rate, δ, is simply the trace of the strain rate tensor

$$\delta = E_1 + E_2. \tag{12}$$

[18] We use the dilatation rate as a proxy for extension even though we are only looking in two dimensions (in three dimensions, dilatation is the volumetric change). The rotation rate, ω, comes from the rotation rate tensor in equation (4) and is defined as

$$\omega = -\frac{1}{2}\left(e_{xy} - e_{yx}\right) \tag{13}$$

where positive values of ω correspond to counterclockwise rotations.

4. Results

4.1. Baseline Results

4.1.1. Southern Salton Sea

[19] To look at the component of motion in the southern Salton Sea (region 1 in Figure 1, Figure 3a), we compute baselines between continuous GPS station P507 and stations near Bombay Beach (from north to south, G003, D11G, DHLG, BERT, G001, POPE, FRIN, and I025). We rotate the baselines into N50°E (the mean orientation from *Chen and Shearer* [2011]) and N40°W to obtain the fault-parallel and fault-perpendicular directions. The results are shown in Table 1. Excluding the baselines to FRIN and I025, we obtain a weighted mean fault-parallel velocity of 3.65 ± 0.89 mm/yr (left lateral) and extension of 4.72 ± 0.92 mm/yr. We exclude the baselines to FRIN and I025 because they only extend across

Table 1. Baseline Velocity Changes Throughout the Brawley Seismic Zone (SS = Strike-slip, Ext. = Extension)

Site 1	Site 2	SS (mm/yr)	±	Ext (mm/yr)	±
Southern Salton Sea (N50°E)					
G003	P507	4.13	0.71	5.91	0.70
D11G	P507	4.78	1.38	5.69	1.45
DHLG	P507	5.15	0.20	3.76	0.19
BERT	P507	4.95	0.71	1.60	0.76
G001	P507	3.18	0.71	2.59	0.70
POPE	P507	5.59	1.64	2.04	1.71
FRIN	P507	4.75	0.96	3.60	0.99
I025	P507	-0.53	2.16	2.39	2.20
Obsidian Buttes (N65°E)					
VP05	P507	6.67	0.88	0.15	1.01
Q122	P507	4.71	0.44	1.75	0.43
P506	P507	3.70	0.21	3.74	0.20
I029	P507	3.13	1.10	0.51	1.24
VP06	P507	5.65	1.37	3.17	1.66
Central Brawley Seismic Zone (N40°E)					
KALI	ACU2	0.98	1.90	-0.51	1.90
I032	ACU2	3.26	2.03	3.80	2.00
P499	ACU2	2.24	1.06	2.15	1.05
MRM1	ACU2	2.76	2.40	3.23	2.32
KALI	P495	0.65	1.05	-2.69	1.05
I032	P495	3.58	1.18	5.98	1.15
P499	P495	2.57	0.21	4.33	0.21
MRM1	P495	3.09	1.55	5.41	1.47
KALI	VP04	-2.07	1.68	-2.29	1.68
I032	VP04	2.16	1.81	1.00	1.78
P499	VP04	-1.14	0.84	0.65	0.84
MRM1	VP04	1.66	2.18	0.43	2.10
Mesquite Basin (N50°E)					
A35	1225	0.41	0.52	3.31	0.53
C35	1225	0.38	0.91	3.81	0.85
D34	1225	0.92	0.49	3.96	0.49
Northern Imperial Fault (N35°W)					
A35	P498	6.10	0.30	0.25	0.30
C35	P498	6.60	0.60	0.16	0.71
D34	P498	6.80	0.26	0.70	0.27
A35	P744	6.72	0.34	1.63	0.33
C35	P744	7.22	0.64	1.55	0.75
D34	P744	7.42	0.29	2.08	0.31
A35	IVCO	5.08	0.30	-0.35	0.31
C35	IVCO	5.58	0.60	-0.43	0.72
D34	IVCO	5.78	0.26	0.10	0.28
Brawley Fault (N2°W)					
A35	A31	4.83	1.33	0.08	0.99
C35	A31	4.46	1.52	0.42	1.51
D34	A31	4.00	1.27	0.08	0.98
A35	B31	2.05	0.44	-0.34	0.44
C35	B31	1.68	0.63	0.00	0.96
D34	B31	1.22	0.38	-0.34	0.43
A35	D30	2.48	0.42	0.06	0.40
C35	D30	2.11	0.61	0.39	0.92
D34	D30	1.65	0.36	0.06	0.39
A35	D29	1.72	0.39	0.21	0.45
C35	D29	1.35	0.58	0.55	0.97
D34	D29	0.89	0.33	0.21	0.44

part of the zone of deformation and therefore give a constraint as to the southern extent of motion. The baseline between FRIN/I025 and P507 indicates that most of the deformation across the southern Salton Sea is accommodated between FRIN and I025, with a small amount of extension occurring south of I025. This shows that the deformation of the southern Salton Sea is almost completely localized in the region encompassed by the 2009 Bombay Beach seismic swarm. The small amount of extension that exists between I025 and P507 can possibly be explained by northwest trending lineaments (i.e., Wister Fault) along the eastern edge of the Salton Sea, an area dominated by mud volcanoes and mud pots [*Lynch and Hudnut*, 2008]. This is generally thought of as a diffuse continuation of the San Andreas Fault that has become somewhat dormant but still probably accommodates a small amount of strike-slip motion on the order of a few millimeters per year as opposed to ~15–25 mm/yr along the southern San Andreas Fault [*Fialko*, 2006; *Lindsey and Fialko*, 2013].

4.1.2. Obsidian Buttes

[20] The Obsidian Buttes Fault (region 2 in Figure 1, Figure 3b) is dominated by mostly left-lateral shear with a small amount of normal motion, leading to subsidence near P507. We investigate the baseline length change between P507 and VP05, Q122, I029, and VP06 (Table 1). The weighted mean velocities are 4.38 ± 0.80 mm/yr of fault-parallel motion and 2.62 ± 0.91 mm/yr of extension. Projecting this extension onto a fault dipping 72° to the north as indicated by *Lohman and McGuire* [2007] from seismic relocations gives 8.1 ± 3.0 mm/yr of subsidence and 8.5 ± 3.1 mm/yr of dip-slip motion (in the normal direction). This amount of interseismic loading is high compared to the 15 year seismic recurrence interval of *M*5 earthquakes on the Obsidian Buttes Fault [*Reasenberg and Jones*, 1994]; although, as suggested by *Lohman and McGuire* [2007], a significant portion of slip in this region is aseismic. In the case of the 2005 Obsidian Buttes swarm, *Lohman and McGuire* [2007] inferred that the geodetic moment release exceeded the seismic moment release by a factor of 5, which has significant implications for seismic hazard near the southern San Andreas Fault. Our estimated loading rates across a 10 km by 5 km segment of the Obsidian Buttes Fault would indicate a geodetic moment release equivalent to a *M*5.5 earthquake every 15 years. We feel that the deformation across this zone is mostly tectonic rather than hydrologic due to a sharp discontinuity in line-of-sight displacements observed using the permanent scatterer InSAR technique by *Eneva et al.* [2009]. Also, P507 is located directly on top of a Quaternary volcanic dome (Red Hill), limiting the effect of hydrologic compaction that would be more prevalent in a loosely consolidated sedimentary basin [*Robinson et al.*, 1976].

4.1.3. Central Brawley Seismic Zone

[21] The Central Brawley Seismic Zone is a rather broad region of deformation that stretches between the northern termini of the Imperial and Brawley Faults and the Obsidian Buttes Fault. There are three distinct zones of seismicity (region 3 in Figure 1, Figure 3c); however, we only focus on the zone where the 2012 Brawley seismic swarm was located due to the lack of baseline measurements across the southern (between 1225 and KALI) and northern (between VP04, VP05, and VP03) zones. Baselines are computed between stations KALI, I032, P499, and MRM1 on the southern end of the Central Brawley Seismic Zone and stations ACU2, P495, and VP04 on the northern end of the Central Brawley Seismic Zone (Table 1). We find that the baseline length changes between KALI and the three northern stations (ACU2, P495, and VP04) are drastically different from the baseline changes between the northern stations and the other three southern stations, indicating that the majority of deformation is localized to the area just south of VP04. We also see a dropoff in the fault-

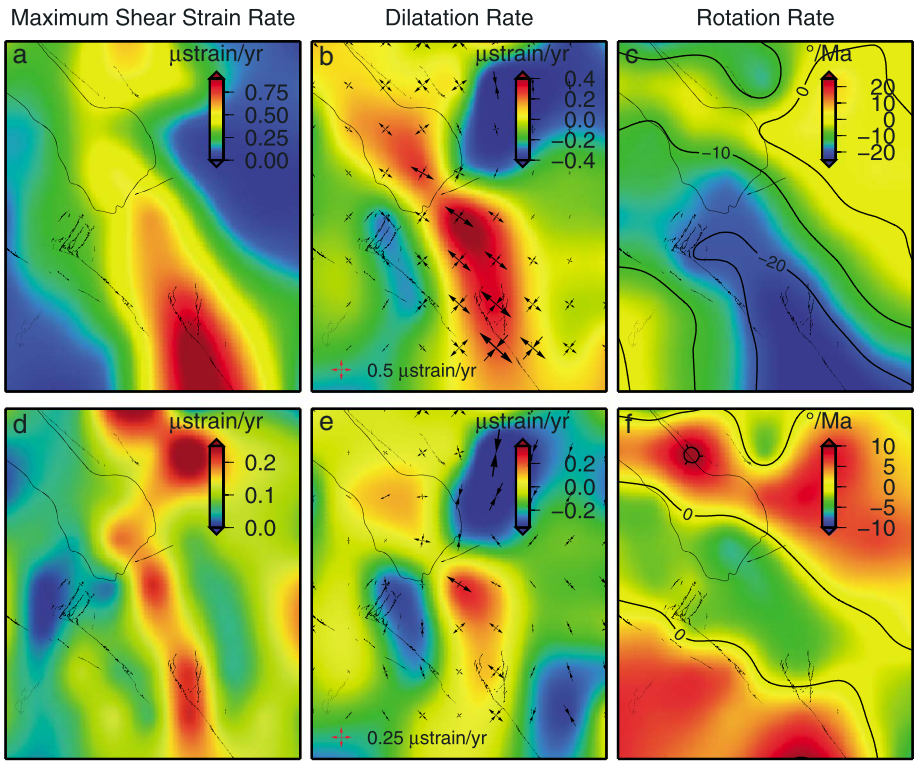

Figure 4. The (left) maximum shear strain, (middle) dilatation, and (right) rotation rates for (a–c) the total velocity field and (d–f) the local velocity field. Positive rotation rates denote counterclockwise rotation. Contour lines on the rotation rate plots (Figures 4c and 4f) show the transition from positive to negative rotation rates. Strain crosses of the orientation and magnitude of the principal strains are shown for the total velocity field in Figure 4b and the local velocity field in Figure 4e.

perpendicular motion for the baselines between VP04/P499 and VP04/MRM1, signifying that those baselines pass through the eastern extent of deformation. Excluding KALI and the two eastern baselines, we obtain a weighted mean left-lateral motion of 2.69 ± 1.46 mm/yr and extension of 4.04 ± 1.43 mm/yr.

4.1.4. Mesquite Basin

[22] The Mesquite Basin is bounded by the Imperial Fault to the west and the Brawley Fault to the east. The interactions between these two faults cause a natural extensional basin due to the relative right-lateral motions. We have three baselines between 1225 and A35, C35, and D34 (Table 1), traversing the entire north-south extent of the basin (region 4 in Figure 1, Figure 3d). We find left-lateral strike-slip motion of 0.61 ± 0.64 mm/yr and extension of 3.69 ± 0.62 mm/yr. The relative absence of strike-slip faulting is seen in moment tensor solutions for larger events in the Mesquite Basin [*Chen and Shearer*, 2011]. The dominance and magnitude of extension in the Mesquite Basin can be explained simply by the relative motion of the Brawley Fault to the Imperial Fault. *Lyons et al*. [2002] estimated that fault creep on the southern Imperial Fault is ~9 mm/yr but drops to ~6 mm/yr in the vicinity of the Brawley Fault. The remaining fault creep is accommodated by the Brawley Fault, which is roughly the amount of extension we see in the Mesquite Basin. When we look at baselines that traverse the Brawley Fault directly (A35, C35, and D34 to A31, B31, D30, and D29), we see 1.92 ± 0.69 mm/yr of right-lateral fault creep, directly in line with estimates from *Lyons et al*. [2002]. Moreover, baselines that traverse the Imperial Fault (A35, C35, and D34 to P498, P744, and IVCO) indicate 6.34 ± 0.40 mm/yr of right-lateral fault creep, further verifying the *Lyons et al*. [2002] results and indicating that the measured interseismic deformation is steady state. It should be noted that the baselines traversing the Brawley and Imperial Faults indicate no fault-perpendicular motion. We estimate that the extension within the Mesquite Basin corresponds to 13.8 ± 3.0 mm/yr of subsidence (using a 75° dip angle estimated from *Chen and Shearer* [2011]), which is roughly in line with estimates of vertical creep since the 1970s along the Brawley Fault from fault trenching by *Meltzner et al*. [2006].

4.2. Strain Rate Results

[23] Maximum shear strain, dilatation, and rotation rate changes are shown in Figure 4 using the total velocity field and the local velocity field (difference of total velocity field and block model of *Smith-Konter and Sandwell* [2009]). The most prominent feature in the strain rate fields is the large shear strain (0.9 μstrain/yr) in the total field associated with the strain localization on the Imperial Fault and a large dilatation (0.2 to 0.5 μstrain/yr) in the Central Brawley Seismic Zone. The strain becomes diffuse as it is partitioned between the San Andreas and San Jacinto Faults, down to between 0.25 and 0.5 μstrain/yr. This is roughly the amount of total engineering strain found through trilateration by *Anderson et al*. [2003]. Also of note is that *Anderson et al*. [2003] reported a dilatation of 0.18 μstrain/yr near Obsidian Buttes, well in the range of values obtained in our study. Strong negative dilatational lobes

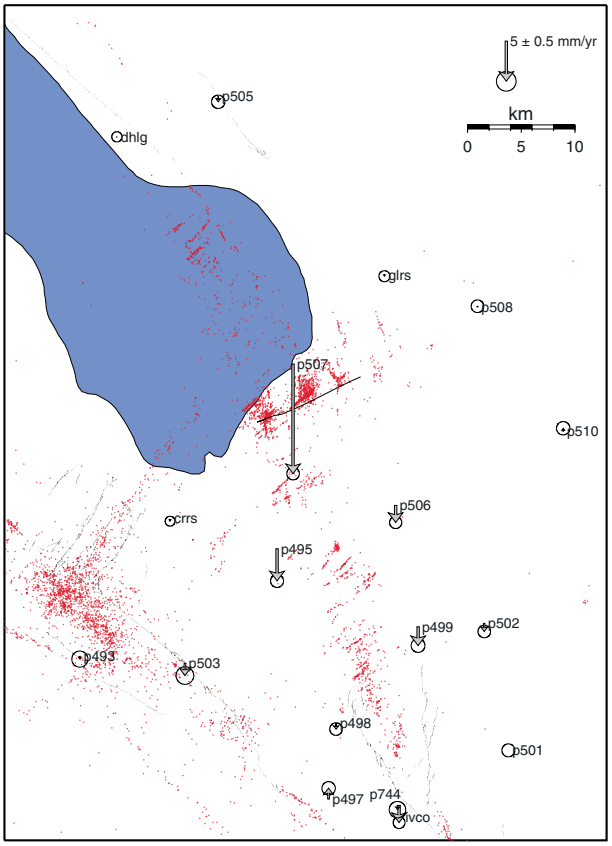

Figure 5. Interseismic vertical velocities for the continuous GPS stations in the Salton Trough. Error ellipses are plotted at the 95% confidence level.

are present near the Chocolate Mountains to the east of the Salton Sea and the Fish Creek Mountains to the west of the Salton Sea, encompassing the Superstition Hills Fault in both the total and local velocity fields, indicative of compression. In the Central Brawley Seismic Zone, 72% of the shear strain rate is explained by the block model, the lowest rate in the region, whereas on the outskirts of the region, more than 90% of the shear strain rate is explained by the block model. Note that using only the continuous GPS velocities yields a highly blurred view of the strain rate estimates in the Salton Trough and that the campaign measurements greatly increase the resolution of the computed strain rate field.

[24] Using the local velocity field, rotation rate throughout the Salton Trough varies rapidly through the Brawley Seismic Zone from ~10°/Ma of clockwise rotation in the Brawley Seismic Zone to ~10°/Ma of counterclockwise rotation to the east and west of the Brawley Seismic Zone. This is clearly demonstrated when looking at the total velocity field in Figure 2, which shows a transition from clockwise to counterclockwise rotation going east across the Brawley Seismic Zone. Also of note is the 10°/Ma of counterclockwise rotation east of the Imperial and Superstition Hills Faults in the local velocity field. This transition is in general agreement with the observed right-lateral motion across the San Andreas Fault and other faults striking northwest. Looking just at the local velocity field, clockwise rotation of 5°/Ma is centered on the Mesquite Basin and the Central Brawley Seismic Zone. This signal is qualitatively confirmed when looking at the ratio of extension to shear in the region. The highest ratio of extension to shear is in the southern Brawley Seismic Zone and tapers off to more shear than extension in the northern Brawley Seismic Zone. The high dilatation rate from the local field also hints at this higher extension to shear ratio in the Central Brawley Seismic Zone. Finally, we want to emphasize that all of the strain rate features persist using both the total and the local velocity fields, indicating that deviations in the assumed fault positions from their true positions in the block model do not cause anomalous strain rate features.

4.3. Vertical Deformation Results

[25] From the baseline measurements, we obtained 4.72 ± 0.92, 2.62 ± 0.91, 4.04 ± 1.43, and 3.69 ± 0.62 mm/yr of extension in regions 1–4, respectively. Figure 5 shows the vertical interseismic velocity field for the continuous GPS stations in the Salton Trough. We ignore the vertical signals for the campaign measurements since they are much noisier than those for the continuous stations. A first-order observation is that the majority of vertical signals are localized within the Brawley Seismic Zone and are indicative of subsidence. The maximum subsidence signal is at site P507 (-13.68 ± 0.32 mm/yr), which is located on a graben between the Obsidian Buttes Fault and faults in the southern Salton Sea. Subsidence at P507 is likely due to a combination of normal faulting to the north and south of the station and possibly water extraction at the nearby geothermal plants [*Chen and Shearer*, 2011]. Furthermore, using the permanent scatterer InSAR technique yields a large spatially coherent subsidence signal along the Obsidian Buttes Fault between 10 and 20 mm/yr [*Eneva et al.*, 2009]. Stations P506, P499, and P502 are outside of the zone of seismicity through the Central Brawley Seismic Zone, and their vertical velocities are -2.12 ± 0.31, -2.34 ± 0.35, and -1.02 ± 0.32 mm/yr, respectively. Station P495 is between the Central Brawley Seismic Zone and the Obsidian Buttes Fault, which explains the slightly higher vertical velocity of -4.00 ± 0.33 mm/yr. Due to this difference, we can attribute ~2 mm/yr of subsidence to the faults in the Central Brawley Seismic Zone, a reasonable value given the diffuse nature of seismicity throughout this zone. This is in general agreement with InSAR line-of-sight velocities in the Central Brawley Seismic Zone (~5 mm/yr) [*Eneva and Shanker*, 2007]. While the extension through the Central Brawley Seismic Zone is about 4 mm/yr, it is probably distributed across many faults that each accommodates only a fraction of that amount, lending to smaller localized subsidence as in the case of P495.

[26] The vertical deformation along the Obsidian Buttes Fault is sharp as indicated by the large subsidence at P507. If we assume that the zone-wide subsidence is ~2 mm/yr (roughly the amount at P506, P499, and P502), then P507 is undergoing ~11–12 mm/yr of subsidence due to faulting on the Obsidian Buttes Fault and faults in the southern Salton Sea. From the horizontal baseline changes, we estimated 8.1 ± 3.0 mm/yr of subsidence along the Obsidian Buttes Fault, which leaves between 3 and 4 mm/yr of subsidence accommodated along faults in the Salton Sea. However, from the baseline changes, we show that most of the deformation in the southern Salton Sea is occurring north of I025. Since elastic deformation attenuates at approximately $1/r^2$, where r is distance to the slipping fault, one would expect a factor of 2 or 3 more vertical deformation localized under the sea,

consistent with findings from other studies [*Brothers et al*., 2009]. The lack of vertical deformation at DHLG indicates that the effects of faulting cease to exist well before the starting point of the San Andreas Fault, and deformation is much more strongly localized than previously estimated.

5. Implications of Rotation of the Brawley Seismic Zone

[27] The clockwise rotation of the Brawley Seismic Zone (Figure 4c) qualitatively explains the left-lateral conjugate faults such as the Obsidian Buttes and the Elmore Ranch Faults, transpression at the southern end of the San Andreas Fault, and transtension in the Mesquite Basin. This of course is a simplification, and the upper crust in the Imperial Valley consists of a highly fractured medium that accomodates the relative motion through left-lateral faulting and extension. However, even this simple interpretation can explain the general features of deformation in the region.

[28] The observed rotation of the Brawley Seismic Zone disappears abruptly approaching the San Andreas Fault, indicating that the San Andreas and San Jacinto Faults are creating an overall extension across the Salton Sea as evidenced by similar geologic and geodetic slip rates along those two faults [*Rockwell et al*., 1990; *Meade and Hager*, 2005; *Behr et al*., 2010; *Janecke et al*., 2010; *Lindsey and Fialko*, 2013]. In case of a small counterclockwise rotation of the eastern part of the Brawley Seismic Zone (Figures 4c and 4f), discrete faults may open and accommodate the rotation through extension and left-lateral shear. The eastward motion of stations east of the Imperial Fault in Figure 2c is evidence for the counterclockwise rotation of the eastern Brawley Seismic Zone. This model is supported by the northwesterly migration of the Brawley Seismic Zone as inferred from basement morphology [*Larsen and Reilinger*, 1991]. In short, rotation of the Brawley Seismic Zone would need to be accommodated along farther northwestward parallel faults to the Brawley Fault over time given topographic constraints (i.e., no along-fault compression of the Imperial Fault). Coincidentally, the existence of diffuse or extinct lineaments southeast of the San Andreas Fault near Bombay Beach [*Lynch and Hudnut*, 2008] further supports this model for northwestward propagation of the Brawley Seismic Zone. Finally, *Fuis et al*. [1984] show from seismic reflection data cutting across the central part of the Brawley Seismic Zone that the basement rocks become shallower toward the east, which would be a direct result of hinged extension across the area (i.e., more extension to the east than to the west).

6. Conclusions

[29] Using a combination of campaign and continuous GPS measurements and a block model for regional tectonics constrained by the continuous GPS data [*Smith-Konter and Sandwell*, 2009], we investigated deformation through the Brawley Seismic Zone from the Imperial Fault in the south to the San Andreas Fault in the north. Differential strain is localized completely within a 10 km wide band that accommodates 11 mm/yr of left-lateral shear and 15 mm/yr of extension. This amount of extension across the Brawley Seismic Zone is consistent with earlier geodetic studies (e.g., 12 mm/yr by *Bennett et al*. [1996]). Rotating the shear and extension measurements into the strike of the San Andreas Fault yields 17 mm/yr of dextral shear, roughly equivalent to geologic and geodetic slip rates near the southern San Andreas Fault. Clockwise rotation in the Imperial Valley can be explained through hinged oblique extension and may be evidence for northwestward propagation of the Brawley Seismic Zone and the San Andreas fault system. Finally, deformation south of the San Andreas Fault appears to be localized, leading to greater hazard and the possibility of sizeable earthquakes that might act as triggers for great earthquakes on the southern San Andreas Fault.

[30] **Acknowledgments.** We would like to thank members of the three field surveys, especially John Blum, Andrew Barbour, Xiaopeng Tong, Ann Armsby, and Melinda Squibb. We also thank Robert Reilinger and an anonymous reviewer for thoughtful considerations. Continuous GPS data are provided by SCIGN operated by SOPAC and USGS, and PBO operated by UNAVCO. This research was partially supported by SCEC through grant USC/SCEC PO 08098 and 09065, NASA grants NNX09AI67G and NNX09AD23G, and USGS grant G12AS20013.

References

Allmendinger, R. W., R. Reilinger, and J. P. Loveless (2007), Strain and rotation rate from GPS in Tibet, Anatolia, and the Antiplano, *Tectonics*, *26*, TC3013, doi:10.1029/2006TC002030.

Altamimi, Z., X. Collilieux, J. Legrand, B. Garayt, and C. Boucher (2007), ITRF2005: A new release of the International Terrestrial Reference Frame based on time series of station positions and Earth Orientation Parameters, *J. Geophys. Res.*, *112*, B09401, doi:10.1029/2007JB004949.

Anderson, G., D. C. Agnew, and H. O. Johnson (2003), Salton trough regional deformation estimated from combined trilateration and survey-mode GPS data, *Bull. Seismol. Soc. Am.*, *93*, 2402–2414, doi:10.1785/0120030014.

Archuleta, R. J. (1982), Analysis of near-source static and dynamic measurements from the 1979 Imperial Valley earthquake, *Bull. Seismol. Soc. Am.*, *72*, 1927–1956.

Behr, W. M., et al. (2010), Uncertainties in slip-rate estimates for the Mission Creek strand of the southern San Andreas fault at Biskra Palms Oasis, southern California, *Geol. Soc. Am. Bull.*, *122*, 1360–1377, doi:10.1130/B30020.1.

Bennett, R. A., W. Rodi, and R. E. Reilinger (1996), Global Positioning System constraints on fault slip rates in southern California and northern Baja, Mexico, *J. Geophys. Res.*, *101*(B10), 21,943–21,960, doi:10.1029/96JB02488.

Bock, Y., R. Nikolaidis, P. de Jonge, and M. Bevis (2000), Instantaneous geodetic positioning at medium distances with the Global Positioning System, *J. Geophys. Res.*, *105*(B12), 28,223–28,253, doi:10.1029/2000JB900268.

Brothers, D., D. Kilb, K. Luttrell, N. Driscoll, and G. Kent (2011), Loading of the San Andreas fault by flood-induced rupture of faults beneath the Salton Sea, *Nat. Geosci.*, *4*, 486–492, doi:10.1038/ngeo1184.

Brothers, D. S., N. W. Driscoll, G. M. Kent, A. J. Harding, J. M. Babcock, and R. L. Baskin (2009), Tectonic evolution of the Salton Sea inferred from seismic reflection data, *Nat. Geosci.*, *2*, 581–584, doi:10.1038/ngeo590.

Burford, R. O. (1972), Continued slip on the Coyote Creek Fault after the Borrego Mountain earthquakes, The Borrego Mountain earthquake of April 9, 1968, USGS professional paper, P0787, 105–111.

Chen, X., and P. M. Shearer (2011), Comprehensive analysis of earthquake source spectra and swarms in the Salton Trough, California, *J. Geophys. Res.*, *116*, B09309, doi:10.1029/2011JB008263.

Eneva, M., and P. Shanker (2007), Subsidence monitoring in Imperial Valley, California, using satellite radar interferometry, *GRC Transactions*, *31*, 551–554.

Eneva, M., G. Falorni, D. Adams, J. Allievi, and F. Novali (2009), Application of satellite interferometry to the detection of surface deformation in the Salton Sea geothermal field, California, *GRC Transactions*, *33*, 315–319.

Fialko, Y. (2006), Interseismic strain accumulation and the earthquake potential on the southern San Andreas fault system, *Nature*, *441*, 968–971, doi:10.1038/nature04797.

Fuis, G. S., W. D. Mooney, J. H. Healy, G. A. McMechan, and W. J. Lutter (1984), A seismic refraction survey of the Imperial Valley Region, California, *J. Geophys. Res.*, *89*, 1165–1189, doi:10.1029/JB089iB02p01165.

Genrich, J. F., and Y. Bock (2006), Instantaneous geodetic positioning with 10–50 Hz GPS measurements: Noise characteristics and implications for monitoring networks, *J. Geophys. Res.*, *111*, B03403, doi:10.1029/2005JB003617.

Genrich, J. F., Y. Bock, and R. G. Mason (1997), Crustal deformation across the Imperial Fault: Results from kinematic GPS surveys and trilateration of

a densely spaced, small-aperture network, *J. Geophys. Res.*, *102*, 4985–5004, doi:10.1029/96JB02854.

Gutman, S. I., S. R. Sahm, S. G. Benjamin, B. E. Schwartz, K. L. Holub, J. Q. Stewart, and T. L. Smith (2004), Rapid retrieval and assimilation of ground based GPS precipitable water observations at the NOAA Forecast Systems Laboratory: Impact on weather forecasts, *J. Met. Soc. Japan*, *82*, 351–360.

Hanks, T. C., and C. R. Allen (1989), The Elmore Ranch and Superstition Hills earthquakes of 24 November 1987: Introduction to the special issue, *Bull. Seismol. Soc. Am.*, *79*, 231–238.

Hauksson, E., J. Stock, K. Hutton, W. Yang, J. Vidal-Villegas, and H. Kanamori (2011), The 2010 Mw 7.2 El Mayor-Cucapah earthquake sequence, Baja California, Mexico and southernmost California, USA: Active seismotectonics along the Mexican Pacific margin, *Pure App. Geophys.*, *168*, 1255–1277, doi:10.1007/s00024-010-0209-7.

Herring, T. A., R. W. King, and S. C. McClusky (2010), Introduction to GAMIT/GLOBK release 10.4, Mass. Inst. of Technol., Cambridge.

Janecke, S. U., et al. (2010), High geologic slip rates since early Pleistocene initiation of the San Jacinto and San Felipe fault zones in the San Andreas fault system, Southern California, USA, Geological Society of America, Boulder.

Lachenbruch, A. H., J. H. Sass, and S. P. Galanis (1985), Heat flow in southernmost California and the origin of the Salton Trough, *J. Geophys. Res.*, *90*, 6709–6736, doi:10.1029/JB090iB08p06709.

Larsen, S., and R. Reilinger (1991), Age constraints for the present fault configuration in the Imperial Valley, California: Evidence for northwestward propagation of the Gulf of California rift system, *J. Geophys. Res.*, *96*(B6), 10,339–10,346, doi:10.1029/91JB00618.

Lin, G., P. M. Shearer, and E. Hauksson (2007), Applying a three-dimensional velocity model, waveform cross correlation, and cluster analysis to locate southern California seismicity from 1981 to 2005, *J. Geophys. Res.*, *112*, B12309, doi:10.1029/2007JB004986.

Lindsey, E. O., and Y. Fialko (2013), Geodetic slip rates in the southern San Andreas fault system: Effects of elastic heterogeneity and fault geometry, *J. Geophys. Res. Solid Earth*, *118*, 689–697, doi:10.1029/2012JB009358.

Lohman, R. B., and J. J. McGuire (2007), Earthquake swarms driven by aseismic creep in the Salton Trough, California, *J. Geophys. Res.*, *112*, B04405, doi:10.1029/2006JB004596.

Lynch, D. K., and K. W. Hudnut (2008), The Wister mud pot lineament: Southeastward extension or abandoned strand of the San Andreas fault?, *Bull. Seismol. Soc. Am.*, *98*, 1720–1729, doi:10.1785/0120070252.

Lyons, S. N., and D. T. Sandwell (2003), Fault creep along the southern San Andreas from interferometric synthetic aperture radar, permanent scatterers, and stacking, *J. Geophys. Res.*, *108*(B1), 2247, doi:10.1029/2002JB001831.

Lyons, S. N., Y. Bock, and D. T. Sandwell (2002), Creep along the Imperial Fault, southern California, from GPS measurements, *J. Geophys. Res.*, *107*(B10), 2249, doi:10.1029/2001JB000763.

Mason, R. G. (1987), Geomensor surveys in the Imperial Valley, California, Geol. Dep., Imperial College, London.

Meade, B. J., and B. H. Hager (2005), Spatial localization of moment deficits in southern California, *J. Geophys. Res.*, *110*, B04402, doi:10.1029/2004JB003331.

Meltzner, A. J., T. K. Rockwell, and L. A. Owen (2006), Recent and long-term behavior of the Brawley fault zone, Imperial Valley, California: An escalation in slip rate?, *Bull. Seismol. Soc. Am.*, *96*, 2304–2328, doi:10.1785/0120050233.

Reasenberg, R. A., and L. M. Jones (1994), Earthquake aftershocks: update, *Science*, *265*, 1251–1252, doi:10.1126/science.265.5176.1251.

Robinson, P. T., W. A. Elders, and L. J. P. Muffler (1976), Quaternary volcanism in the Salton Sea geothermal field, Imperial Valley, California, *Geol. Soc. Am. Bull.*, *87*, 347–360, doi:10.1130/0016-7606(1976)87 < 347:QVITSS > 2.0.CO;2.

Rockwell, T., C. Loughman, and P. Merifield (1990), Late Quaternary rate of slip along the San Jacinto fault zone near Anza, southern California, *J. Geophys. Res.*, *95*, 8593–8605, doi:10.1029/JB095iB06p08593.

Sharp, R. V. (1967), San Jacinto fault zone in the Peninsular Ranges of southern California, *Geol. Soc. Am. Bull.*, *78*, 705–730.

Shearer, P. M. (2002), Parallel fault strands at 9-km depth resolved on the Imperial Fault, Southern California, *Geophys. Res. Lett.*, *29*(14), 1674, doi:10.1029/2002GL015302.

Shen, Z.-K., D. D. Jackson, and B.-X. Ge (1996), Crustal deformation across and beyond the Los Angeles basin from geodetic measurements, *J. Geophys. Res.*, *101*(B12), 27,957–27,980, doi:10.1029/96JB02544.

Sillard, P., Z. Altamimi, and C. Boucher (1998), The ITRF96 realization and its associated velocity field, *Geophys. Res. Lett.*, *25*, 3223–3226, doi:10.1029/98GL52489.

Smith-Konter, B., and D. Sandwell (2009), Stress evolution of the San Andreas fault system: Recurrence interval versus locking depth, *Geophys. Res. Lett.*, *36*, L13304, doi:10.1029/2009GL037235.